High Speed Rotor System for a Megawatt-Class Integrated Motor Drive Technology Demonstrator

High Speed Rotor System for a Megawatt-Class Integrated Motor Drive Technology Demonstrator

Yuankang Chen*, Zoltán S. Spakovszky†, Edward M. Greitzer‡, Zachary C. Cordero§,
David G. Cuadrado¶, and Marc Amato‖
Massachusetts Institute of Technology, Gas Turbine Laboratory, Cambridge, MA, 02139

Increasing mechanical speed is a critical pathway to improving electric machine specific power, but challenges include maintaining tight air gap clearances during operation. Even a partial loss in air gap due to a rotor-stator geometric offset produces destabilizing electromagnetic forces that negatively impact rotordynamic stability, in a manner similar to that of fluid pressure forces in turbomachinery. A high-speed rotor system for a megawatt-class motor drive demonstrator is presented, with the rotor structural integrity experimentally validated at rated speed and temperature in a spin pit test. The rotor system utilizes solid dampers (O-rings) to avoid the cost and complexity of fluid dampers, and a novel bearing housing module with an in-situ damper tuning mechanism is designed and tested to mitigate the associated risks.

I. Nomenclature

$\dot{E}$	=	energy dissipation rate (power)
C_d	=	damping coefficient
F_r	=	radially-directed force
F_θ	=	tangentially-directed force
Δx	=	displacement in the x-direction
$\dot{x}$	=	velocity in the x-direction
$\dot{y}$	=	velocity in the y-direction

II. Introduction

The adoption of electric machines for aircraft propulsion requires significant improvements in machine specific power, with air gap speed (the product of machine air gap radius and mechanical speed) identified as a key parameter. Several of the challenges associated with high speed rotors to be addressed include structural integrity (retaining the electromagnetic rotor elements) and operability (maintaining air gap clearance).

For an outer-rotor machine, the electromagnetic rotor elements are retained by a drum, which also acts as the torque-transferring element. High tensile strength is critical to rotor drum performance, and several designs use carbon-fibre sleeves on metallic drums [1] for their exceptional strength-to-weight ratio and stiffness. An unsleeved titanium rotor drum is selected to preserve the possibility of integrating the electric machine with a compressor in a gas turbine (e.g. by installing compressor blades on the rotor outer surface). The rotor drum is successfully tested at design speed and operating temperature in a spin pit, with no signs of plastic deformation or adhesive failure. Additionally, the measured rotor radial growth at design speed is within 10% of that predicted by FEA.

The integrated motor drive unit [2] utilizes an overhung rotor architecture with two angular contact bearings and solid dampers (O-rings), with two units operated in a back-to-back configuration for technology demonstration. Rotordynamic analysis shows the demonstrator rotor system meets requirements, with a separation margin of 52% design speed and >80% design air gap maintained when passing through the criticals during startup and slowdown. A key challenge

*Research Assistant, now working at GE Global Research
†T.A. Wilson Professor of Aeronautics and Astronautics; Head, Air Sector; Director, Gas Turbine Laboratory, 31-317
‡H.N. Slater Professor of Aeronautics and Astronautics, 31-319
§Assistant Professor of Aeronautics and Astronautics, 33-332
¶Research Engineer, 31-316
‖CEO,Innova-Logic LLC, Saunderstown, RI, 02874

for the overhung architecture is the synchronous excitation of the lightly damped spindle modes via the destabilizing electromagnetic rotor-stator forces. This is addressed by increasing the natural frequencies of the spindle modes by stiffening the spindle root with a thick conical connection to the aft frame.

Solid dampers consisting of O-rings are selected to avoid the additional mass and complexity associated with conventional fluid dampers. A key risk associated with utilizing O-rings as dampers is that their stiffness and damping is sensitive to factors including squeeze and temperature [3], and as the system rotordynamic operability is found to be strongly dependent on damper stiffness, a novel bearing housing design with in-situ damper tuning capability is developed. A pair of experiments are planned to mitigate the risks associated with the tunable damper bearing housing design.

III. Rotor Drum Design and Evaluation

Figure 1 shows the three structural components of the electric machine rotor - the rotor drum, retaining ring, and forward end bell. An unsleeved titanium rotor drum is selected to retain the Halbach array magnets. Titanium is selected for its high strength-to-weight ratio, minimizing the required thickness (and hence drum mass). The rotor drum thickness is sized for a structural safety factor of 2 at design speed, expanding 1 mm (or 40 thou) in diameter to achieve the design air gap of 3 mm. The inner surface of the rotor drum has flat slots for the pole magnets, which aids in ensuring consistency in the magnet installation process. The retaining rings control rotor radial growth during operation, and provide a surface for balancing features. The forward end bell has similar balancing features, and a contoured inner surface to direct cooling flow toward the end turns and machine air gap.

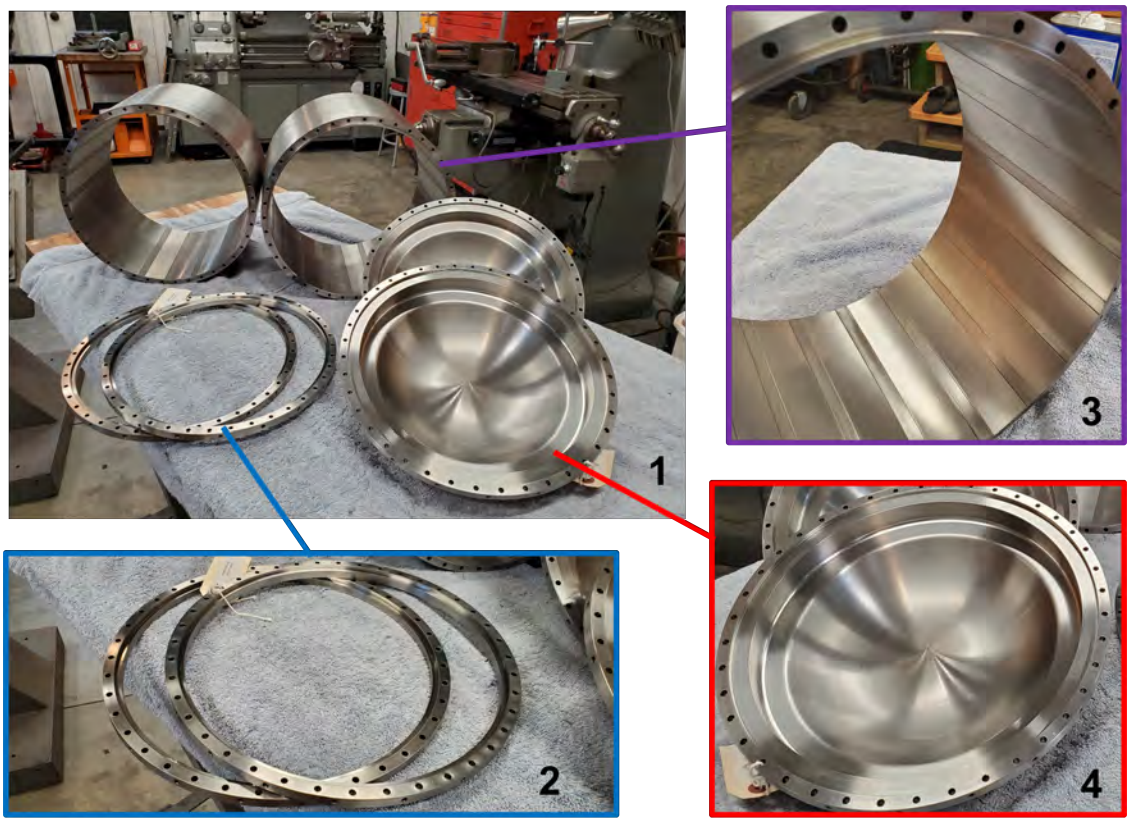

Fig. 1 1) Structural components of two electric machine rotors. 2) Retaining rings. 3) Rotor drum. 4) Forward end bell.

A. Spin Pit Experiment

A spin pit test of the rotor drum, retaining ring, and forward end bell was conducted to address the following key risks:

- Loss of structural integrity in the titanium drum, and the adhesive between the drum and magnets during operation. The adhesive between the rotor drum and the magnets is a potential point of failure as it is subject to a combination of compressive loads in the radial direction (from the centrifugal force of the magnets), tensile loads in the tangential direction (due to rotor radial growth), and shear loads (from torque transfer to/from the magnets). Maintaining adhesive strength through exposure to elevated magnet temperatures over repeated loading cycles is another key challenge.
- Damage to the electric machine and bearings due to excessive vibrations during acceleration up to and operation at design speed.
- Reduction in electromagnetic torque production due to excessive increase in air gap during operation (a result of rotor radial expansion under centrifugal loading).

Results from electromagnetic FEA show that at operating speed and torque, the magnetic forces on the magnets (which are then transferred to the rotor) are small compared to the centrifugal forces. Thus, the presence of an energized stator in the spin pit test is unnecessary. One row of magnets is installed on the rotor drum, and the remaining rows filled with steel blocks of equivalent mass to the magnets. Figure 2 shows the rotor drum used in the spin pit test, with a minor depression over the row of magnets in the right picture (the steel blocks are 10% thicker than the magnets as they are 10% less dense). Figure 3 shows the rotor assembly being balanced and installed in the spin pit. The rotor is powered by an air turbine, and the vibrations are measured at the spin arbor.

Fig. 2 Rotor drum (left) with rows of steel blocks (middle) and one row of magnets (right) used in spin pit test

The spin pit experiment procedure was conducted at Barbour Stockwell Incorporated (BSi) with the following procedure:

1) The dimensions and the unbalance of the rotor assembly are measured before the experiment.
2) The rotor assembly is then installed in the spin pit and accelerated to 70% of the design speed, where it dwells for 1 minute. During this time, the geometry measurements and vibrational data is recorded.
3) The rotor assembly is then brought to a halt, and its dimensions and unbalance are measured to determine if plastic deformation has occurred.
4) If no plastic deformation has occurred, the two prior steps are repeated, with the rotor assembly brought up to 80%, 90%, and then 100% of design speed, then brought to a halt and re-measured.
5) The 100% design speed experiment is then repeated at elevated temperature* and conducted over the course of an hour. In addition to the geometry and vibrational measurements, the temperature of the rotor drum is measured

*To account for the impact of elevated magnet temperatures (due to eddy current losses during operation) on the structural strength of the rotor drum and the bond strength of the adhesive, the spin pit test is conducted with the rotor assembly at 100 °C. This is a conservative estimate as thermal models estimate the magnet hotspot to be 75 °C.

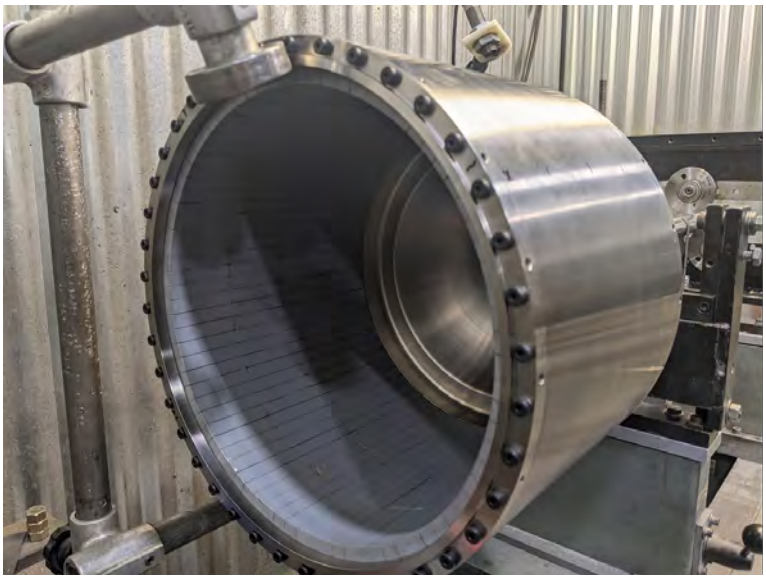

Fig. 3 Rotor drum undergoing balancing (left) and installed in a spin pit (right)

via a thermocouple.

The vibration response in the ambient and elevated temperature experiments are shown in Figure 4. In both experiments, only the first conical mode is crossed (at approximately 30% design speed), and vibration magnitude remains steady at speed. The maximum radial growth in rotor drum diameter (occurring at the axial center of) at design speed was measured during the experiment to be 35-37 mils, which is within 10% of that predicted via FEA (40 mils or 1 mm). The rotor was inspected after the spin pit test, and no sign of damage to the rotor drum or adhesive was detected.

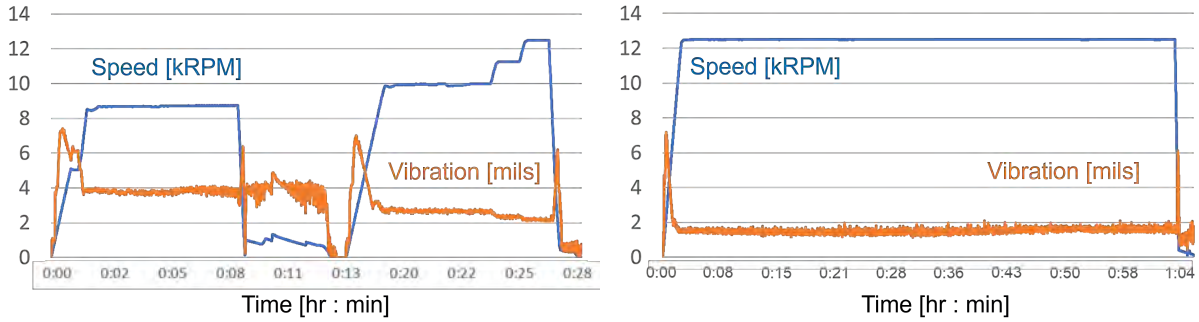

Fig. 4 Rotor vibrations held steady at ambient (left) and heated (right) conditions (figure courtesy of Barbour Stockwell)

IV. System Rotordynamics

To avoid damage due to excessive vibrations and rotor-stator contact, the rotor system is required to have a minimum separation margin of 30% design speed and maintain a >75% electric machine air gap during operation at rated speed and startup and slowdown transients. The rotor system is operated supercritically, and damping is key to crossing the rigid body modes safely.

A. Rotor Architecture

The rotordynamic analysis presented in this chapter is conducted with reduced order models utilizing a direct stiffness lumped parameter method originally developed by Spakovszky [4]. Shafts[†] are modelled as a series of thin rigid disk elements (lumped masses) connected by flexible beam elements.

Figure 5 illustrates the back-to-back motor drive demonstrator system layout and its reduced order model representation. The generator supplies DC electrical power to the motor, and the motor shaft power to the generator, and an external 150 kW power supply makes up for the system losses. This configuration minimizes the size of the external power supply required to operate the demonstrator. The green boxes enclosing the rotor and spindle represent the electromagnetic interactions between machine stator and rotor, which are modelled as direct and cross-coupled stiffnesses. Air flows through the hollow spindle before entering the heat exchanger and electric machine, and the overhung rotor architecture is selected to preserve the maximum available cooling flow area.

The Campbell diagram and first three pairs of modes are shown in Figure 6. The first rigid body mode is shown in Figure 7. Each line in the figure represents the centerline of a shaft, with the dots representing the lumped mass nodes. Multiple instances of each shaft at various timestamps are superimposed on the figure to visualize the mode, which in the case of Figure 7 is the rotor conical mode. The dashed black lines represent intershaft connections, comprising bearings, rotor-stator electromagnetic interactions, and couplings. The dashed red lines represent connections of the structure to ground.

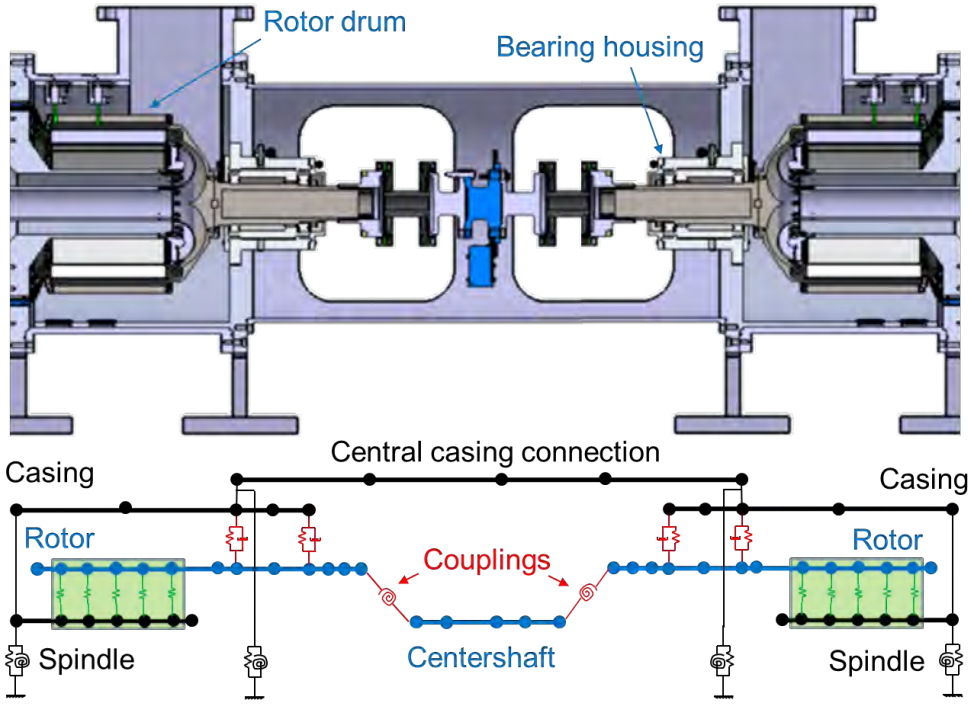

Fig. 5 Motor drive demonstrator geometry (top) and corresponding rotordynamic model (bottom)

B. Destabilizing Electromagnetic Rotor-Stator Forces

A local reduction in the electric machine air gap increases local electromagnetic forces (rotor-stator attraction and torque production). Figure 8 shows conceptually how an offset in the x-direction between rotor and stator centerlines produces local variations in force magnitudes that yield both a direct-coupled force in x and a cross-coupled force in y on the rotor. This cross-coupling can induce rotor whirl in operation. These forces produce a destabilizing effect on the rotor system, and must therefore be captured in the rotordynamic analysis. Electromagnetic FEA conducted by Dowdle [5] shows the magnitudes of these forces scale approximately linearly with rotor displacement, and the impact of a

[†]The nonrotating cylindrical components of the motor drive, such as the spindle or casing elements, are modelled as shafts with a rotational speed of zero.

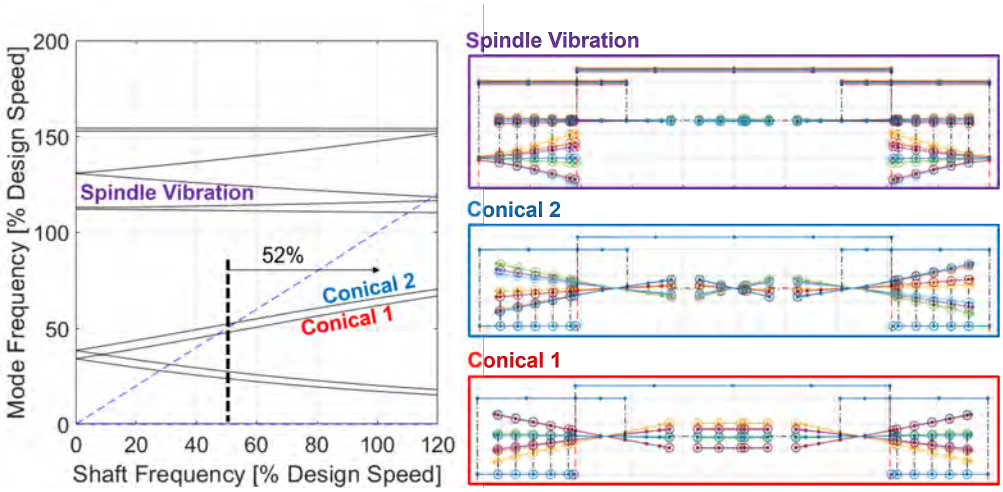

Fig. 6 Campbell diagram (left) and system mode shapes (right)

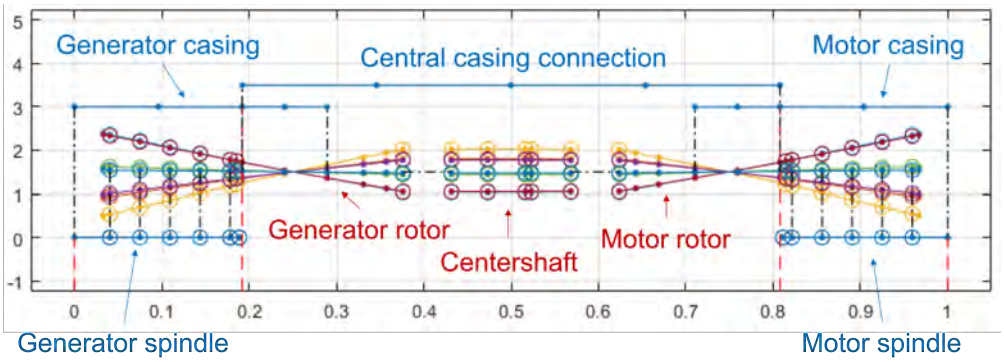

Fig. 7 Mode shape diagram for first rigid body mode

geometric offset (due to rotor and stator displacements during operation) is modelled as a combination of direct and cross-coupled stiffnesses between machine rotor and stator.

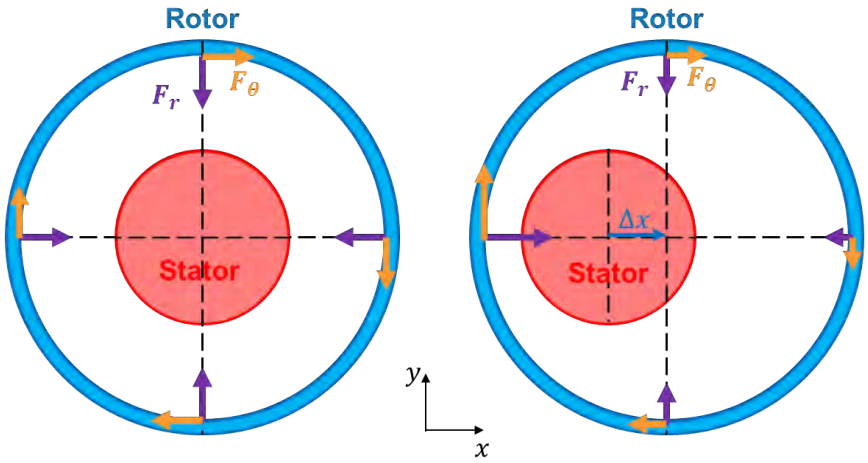

Fig. 8 Net forces on rotor sum to zero in perfectly aligned machine (left), and a shaft offset in the x-direction yields a destabilizing cross-coupled force in the y-direction inducing rotor whirl (right)

C. Quasi-steady Analysis

The unbalance and stackup assumptions of the rotordynamic analysis are the following:

- All rotor components are balanced to G2.5 standard (a conservative assumption as the electric machine rotors are balanced to G1.0 instead)
- The unbalance of all components are distributed in the same direction
- Each mechanical fit produces a 0.5 thou stackup displacement

The rotor system operates supercritically with a separation margin of 52% design speed, and sufficient damping must be included to ensure safe operation during crossing of the rotor conical modes. The overhung rotor architecture results in the electric machine stator and heat exchanger positioned at the end of a cantilevered structure (the spindle), with low levels of damping the stator vibrations. As rotor displacements cause synchronous excitations in the stator due to the destabilizing electromagnetic forces, the natural frequencies of the lightly damped spindle modes must be kept above the operating speed range. In the demonstrator, this is achieved by stiffening the spindle root with a thick conical connection to the aft frame.

A preliminary sizing analysis suggests the amount of damping required is on the order of 1000 Ns/m per damper and could be achieved with solid dampers (i.e. O-rings). Elastomer-based dampers reduce system cost and complexity. Figure 9 shows that the separation margin is sensitive to the damper stiffness: a 50% reduction in damper stiffness results in the full rotor bending modes coinciding with design speed, and a doubling of stiffness reduces separation margin and increases the critical frequencies (and the forces and displacements experienced by the rotor when crossing them).

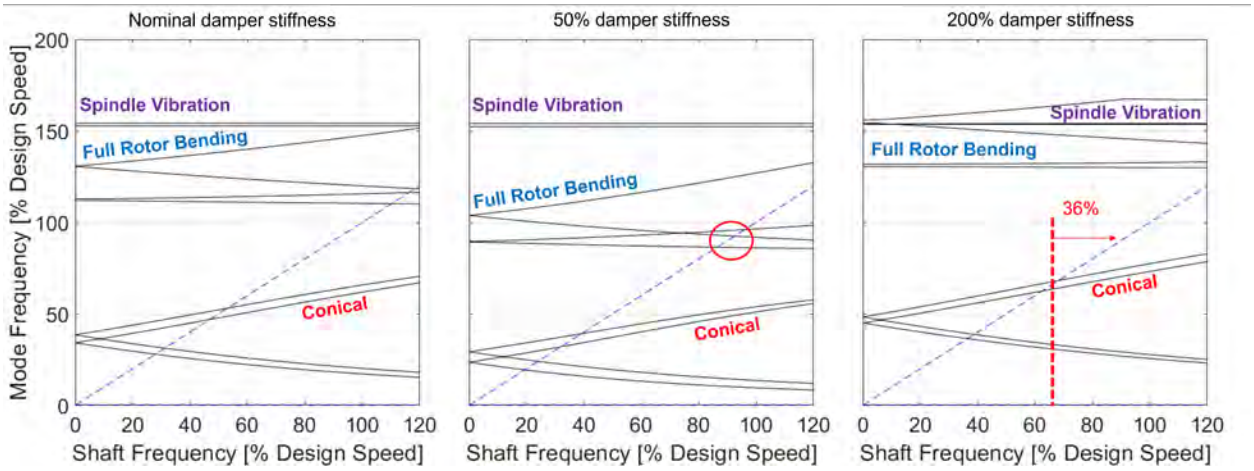

Fig. 9 Shift in rotor conic and bending frequencies due to halving (middle) and doubling (right) of damper stiffness

D. Startup and Slowdown Transients

Transient analyses are conducted to address the following key risks for the demonstrator during startup and slowdown:

- Collision between electric machine rotor and stator due to excessive loss in air gap causing damage to either component
- Vibrational energy dissipated in solid dampers may lead to overheating, leading to change in damper stiffness and damping or damage to dampers
- Radial force loading on diaphragm coupling in excess of structural limits leading to failure

The demonstrator is brought up to speed during the startup transient by operating the motor with the 150 kW power supply (and the generator turned off). The acceleration rate during startup (shown in Figure 10) is set by the motor torque-speed curve with the supplied power. When the demonstrator reaches design speed, the speed will be held steady and generator power slowly raised until nominal operation is achieved.

The demonstrator is brought to a stop without the application of an external brake. Instead, during the slowdown transient (shown in Figure 11), both machines are turned off, with rotor dissipation (in the form of rotor windage and core losses) the only source of deceleration.

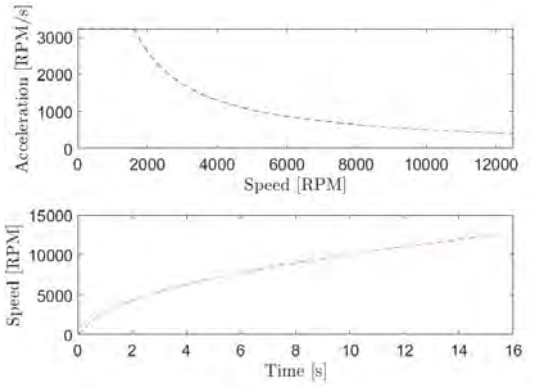

Fig. 10 Startup acceleration rate limited by external power supply

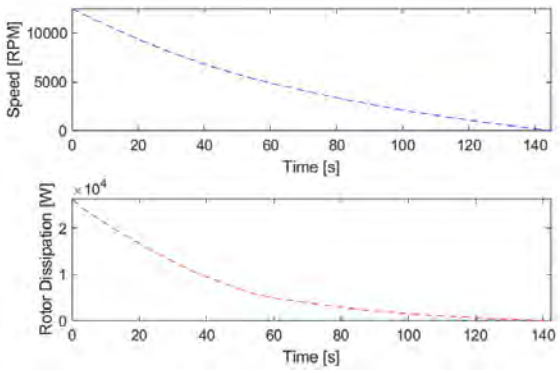

Fig. 11 Slowdown deceleration rate set by rotor dissipation

1. Air Gap Loss and Damper Heating

Figures 12 and 13 show the startup and slowdown transient responses respectively. The increased critical dwell time during slowdown compared to the startup process does result in an increased loss in air gap, but the peak loss is still less than the limit of 25% design air gap.

The energy dissipated within each damper $\dot{E}_d$ is:

$$\dot{E}_d = C_d(\dot{x}_d^2 + \dot{y}_d^2) \tag{1}$$

where C_d is the damper damping coefficient and $\dot{x}_d$ and $\dot{y}_d$ the damper x and y-directed velocities respectively. The damper velocities are assumed to be equal to those of the shaft (as the shaft and bearing radial stiffnesses are much larger than those of the damper).

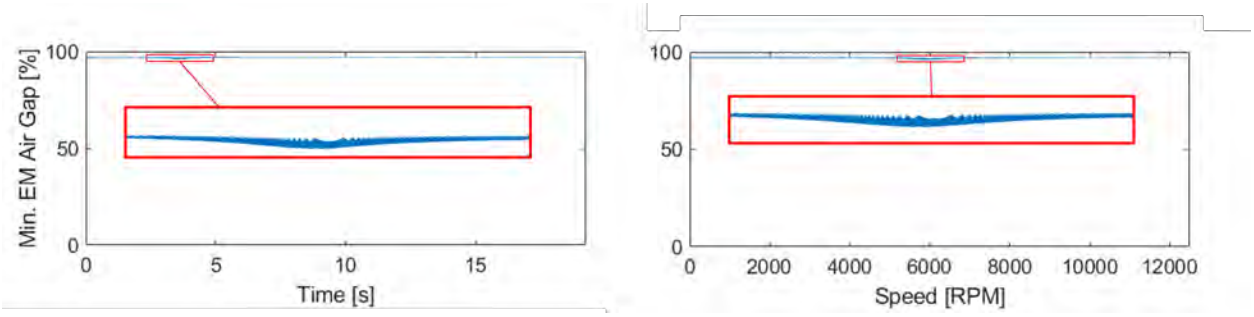

Fig. 12 Startup transient response: minimum EM air gap vs time (left) and minimum EM air gap vs speed (right)

To estimate the temperature rise in the dampers due to the heat load, the heat input across the slowdown transient is integrated to determine the total energy input to the damper. Assuming conservatively that:

- The heat input for each damper is isolated to a single O-ring
- All the heat goes into raising the temperature of the O-ring (with no heat removed via external conduction/convection)
- Estimated heat capacity of each Buna-N O-Ring: 8.73 J/K

The resultant damper energy input and temperature increases over the slowdown transient are found to be negligible:

- Generator-side aft damper: 3.57 J energy input yielding 0.4 ℃ increase
- Generator-side forward damper: 0.87 J energy input yielding 0.1 ℃ increase
- Motor-side aft damper: 2.94 J energy input yielding 0.3 ℃ increase
- Motor-side forward damper: 0.65 J energy input yielding 0.1 ℃ increase

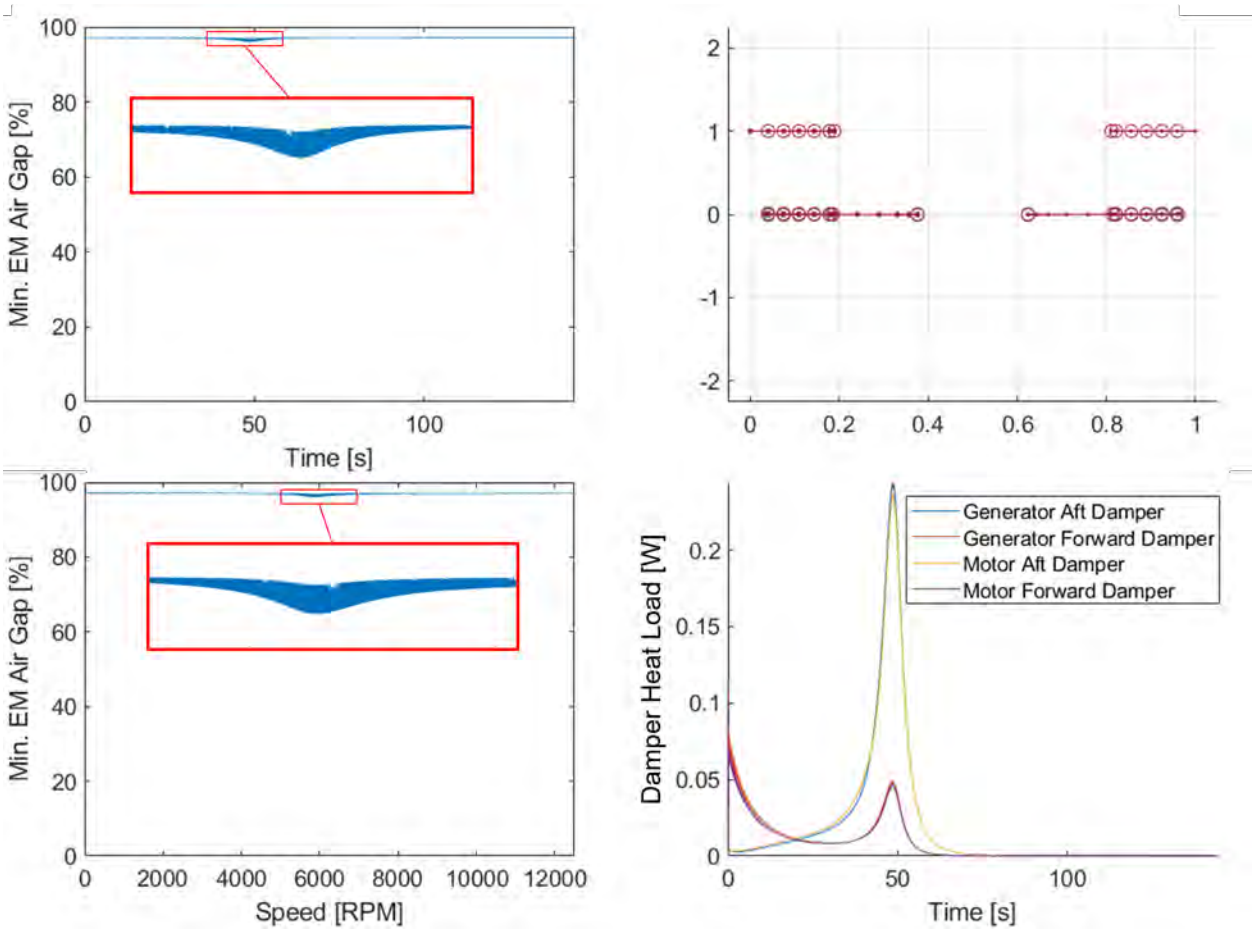

Fig. 13 Slowdown transient response: minimum EM air gap vs time (top left), minimum EM air gap vs speed (bottom left, mode shapes at minimum air gap (top right), damper heat loads vs time (bottom right)

2. Coupling Radial Force Loading

The centershaft (illustrated in Figure 14) is the rotor component connecting the generator and motor driveshafts. It consists of a contactless torquemeter, a pair of diaphragm couplings, and the connecting flanges. Couplings play a critical role in enabling operability of the back-to-back system by accommodating driveshaft axial travel and misalignment. A double-coupling centershaft design is selected as rotordynamic analysis shows it minimizes the number of criticals that must be crossed during startup and shutdown.

The centershaft elements are subject to unbalance forces during operation, and as the shaft is not supported by bearings, these force loads are transferred to machine rotors through the diaphragm couplings. As the diaphragm couplings are not rated for radial loads, there is a risk that these loads may cause structural failure of the couplings, especially when crossing the critical speeds. To address this risk, the force loads are first extracted from the transient rotordynamic analysis. These force loads are then imposed on the coupling diaphragm in FEA, and the resultant stresses checked against the material Goodman line to assess the coupling safety factor.

Figure 15 shows the coupling force loads and maximum centershaft displacement during both startup and slowdown transients. The maximum radial force loading of 100 N is comparable to that of the weight of centershaft elements borne by each coupling (63 N shaft weight split for 32 N per coupling).

Figures 16 and 17 show the FEA setup and results of the steel coupling diaphragm when subjected to a combination of steady centrifugal and torque loading and oscillatory radial force loads. Comparing a linear superposition of the mean stress from torque and centrifugal loads and the alternating stress from radial loads against the Goodman curve from the manufacturer showed the coupling had a satisfactory structural safety factor of 2. Additionally, repeated FEA calculations with varying force loads (the results of which are presented in Table 1) showed the radial force loading

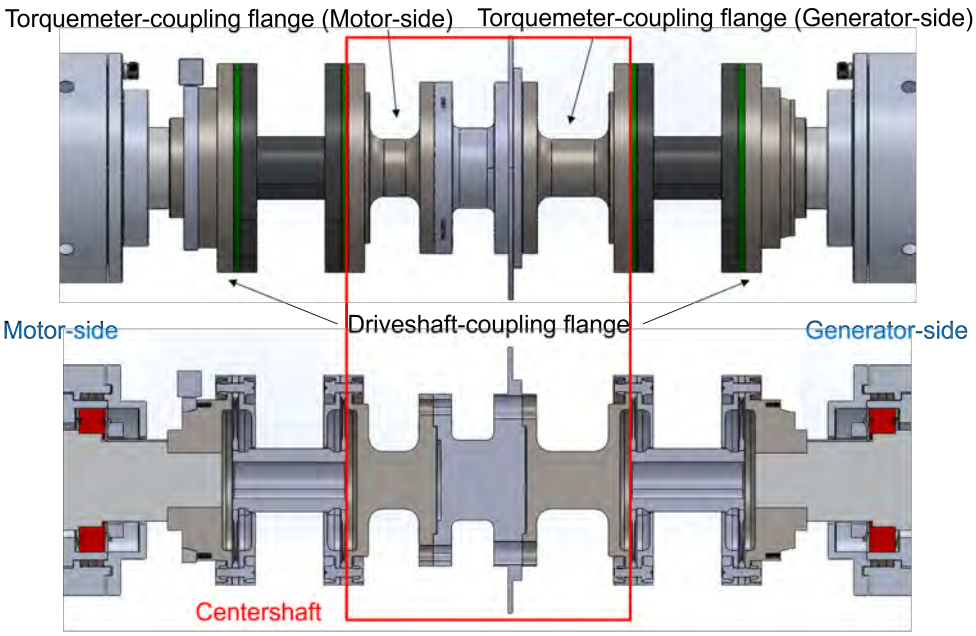

Fig. 14 Double-coupling centershaft design to enable supercritical operation with minimum number of critical frequency crossings

contributes negligibly to the overall coupling stresses.

Centershaft Radial Load (N)	Peak Stress (MPa)	Radial Displacement (mm) [thou]	Angular Deflection (deg)
0	310	0 [0]	0
50	311	0.05 [2]	0.036
100 (Nominal)	311	0.10 [4]	0.072
150	311	0.15 [6]	0.108

Table 1 Coupling FEA results with various centershaft load magnitudes

V. Bearing Housing Design for Tunable Dampers

Solid dampers consisting of O-rings are selected to avoid the additional mass and complexity associated with fluid dampers. The rotordynamic analysis of Figure 6 used scaled-up values of radial stiffness and damping coefficients of O-ring dampers from literature [6], but a key risk associated with utilizing O-rings as dampers is that their stiffness and damping is sensitive to factors including squeeze and temperature [3]. Sensitivity analyses showed the separation margin to be strongly influenced by damper radial stiffness, and thus the ability to adjust or fine-tune the damper stiffness and damping is critical for rotordynamic operability.

Changing the stiffness of a solid damper typically involves replacing one or more O-rings or changing the geometrical dimensions of the damper housing to vary the squeeze (defined as the fractional change in O-ring thickness between its free and installed state). Both processes are costly and complicated, necessitating disassembly and reassembly of the bearing housing module. There is thus a need for the bearing housing design to allow for control over damper stiffness and damping 'in-situ' (i.e. without disassembly).

The tunable damper bearing housing concept leverages the sensitivity of O-ring stiffness and damping to squeeze and a novel O-ring axial compression mechanism to achieve in-situ damper tuning capability. Figures 18 and 19 show the layout of the bearing housing module, and Figure 22 illustrates the operation of the damper tuning mechanism. The bearing carrier, bearings, and driveshaft are fixed relationally to one another and move as a single piece when the bolts

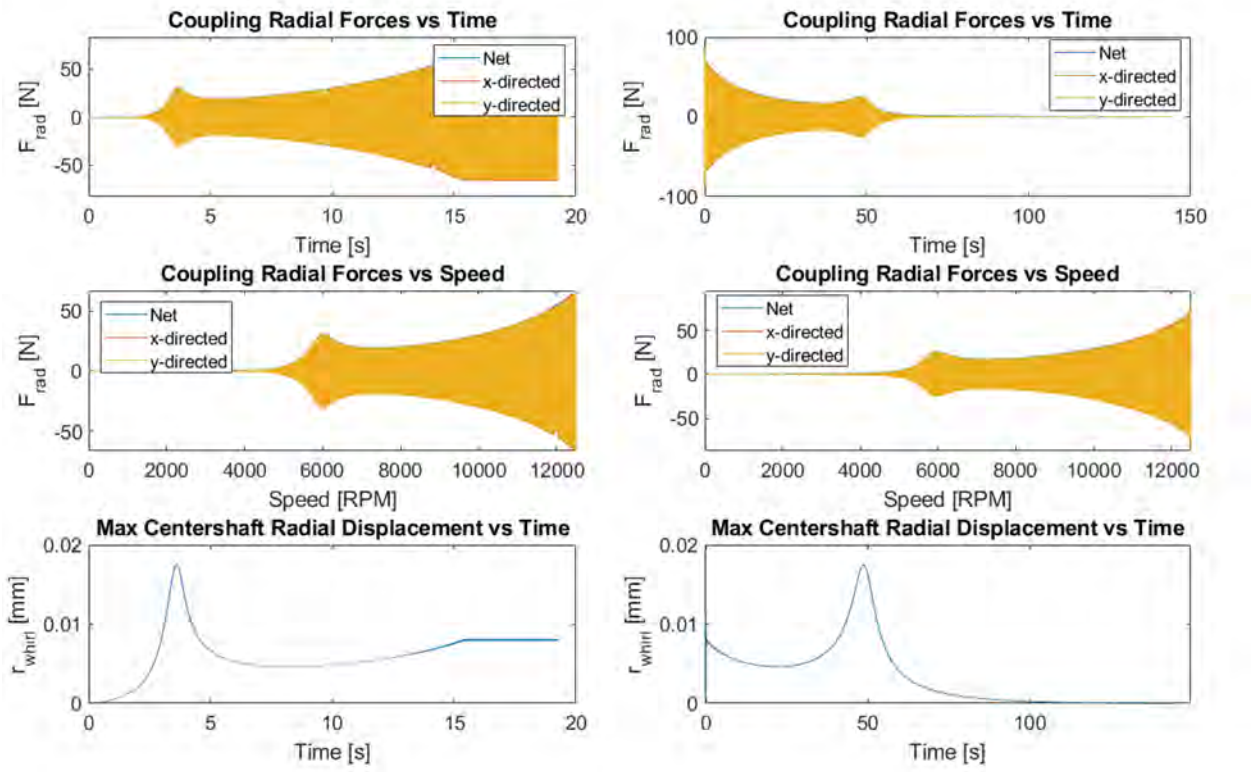

Fig. 15 Coupling force loads and maximum centershaft displacement during startup (left) and slowdown (right) transients estimated to be acceptable

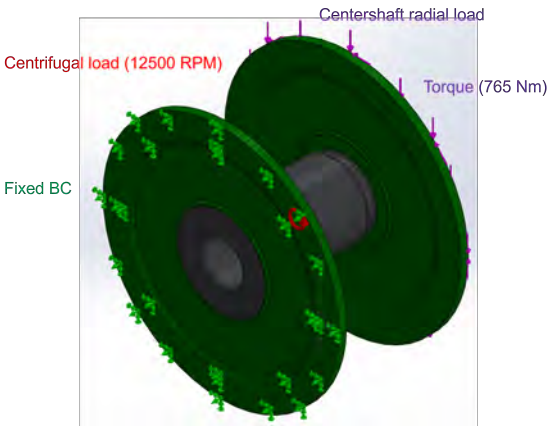

Fig. 16 Coupling diaphragm FEA setup

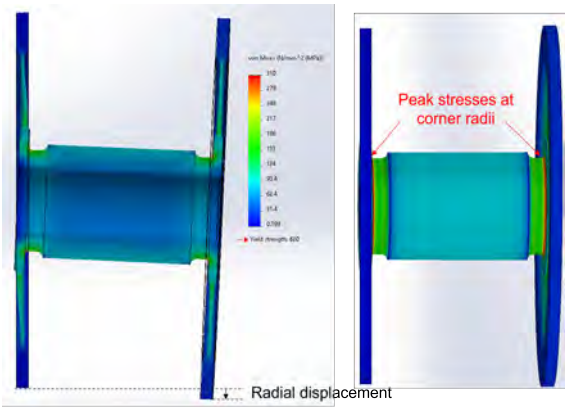

Fig. 17 Coupling diaphragm FEA results (for 100 N radial loading)

are tightened. As O-ring stiffness and damping are sensitive to variations in temperature, a separate air-cooling system (presented in Figure 20[‡]) for the bearing housing module is used for temperature regulation.

A pair of experiments are planned to mitigate risks associated with the novel solid damper system - an experimental characterization of the candidate O-rings for the damper, and a full-scale tuning test for the bearing housing system.

[‡]The inlet and outlet are displaced tangentially by 45 degrees in the final design to minimize the size of the coolant recirculation zone

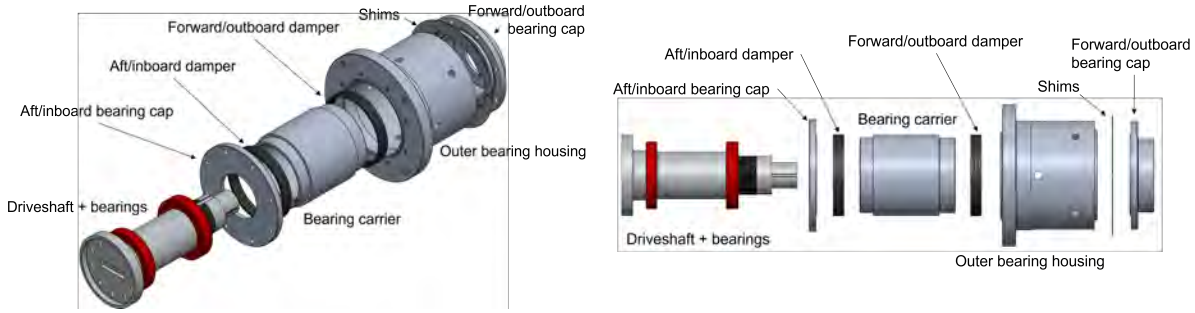

Fig. 18 Isometric (left) and side (right) exploded views of bearing housing module

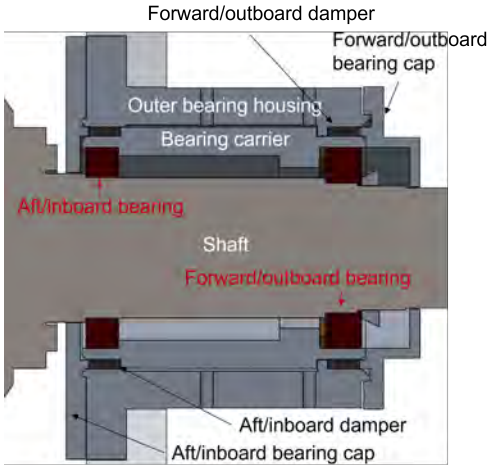

Fig. 19 Cross-sectional view of bearing housing module

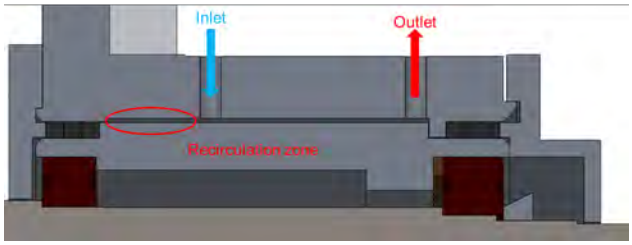

Fig. 20 Bearing housing cooling approach

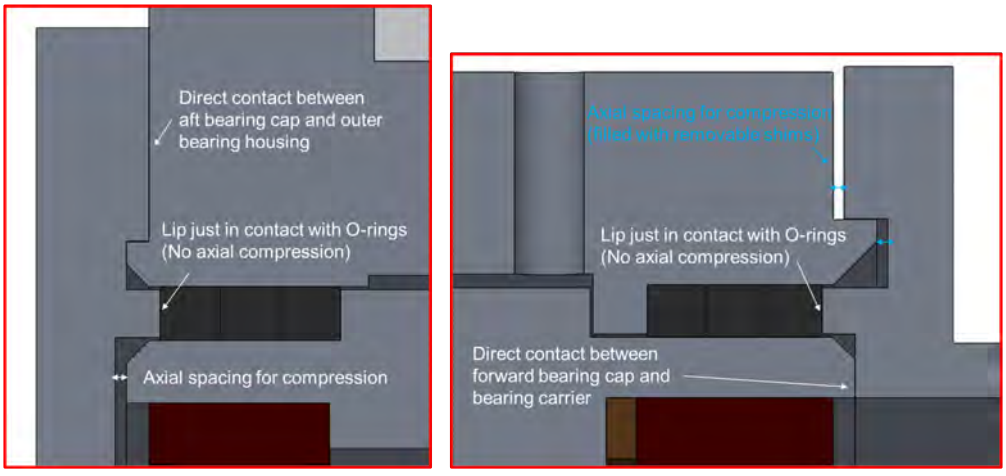

Fig. 21 Forward and aft dampers in axially-uncompressed state

A. Background

Smalley [3] experimentally characterized the stiffness and damping of O-rings across multiple materials, temperature, amplitudes, squeeze and stretch magnitudes, cross-sectional diameters, and groove widths. He found that material choice and radial squeeze are parameters which offer the designer the most direct control over the dynamic characteristics of an

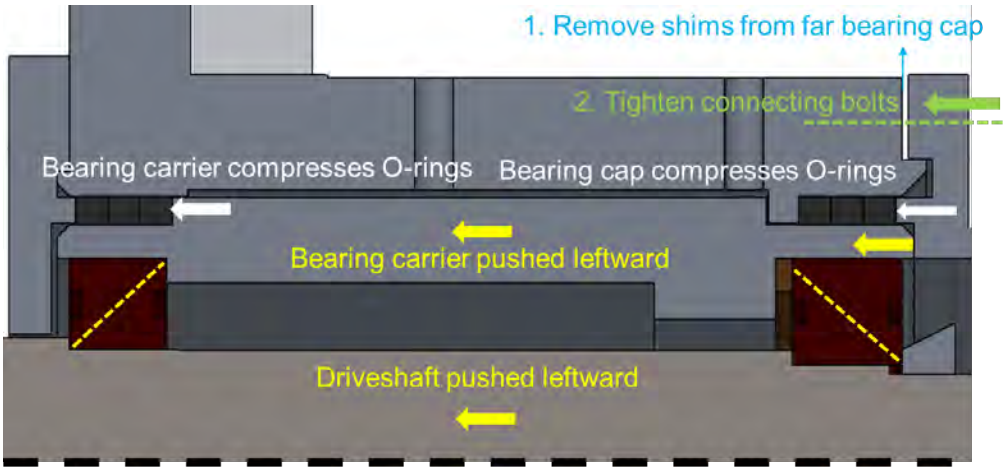

Fig. 22 Damper in-situ tuning mechanism

O-ring. Additionally, temperature and vibration amplitude have a strong effect on O-ring dynamic characteristics and must be carefully accounted for in the design.

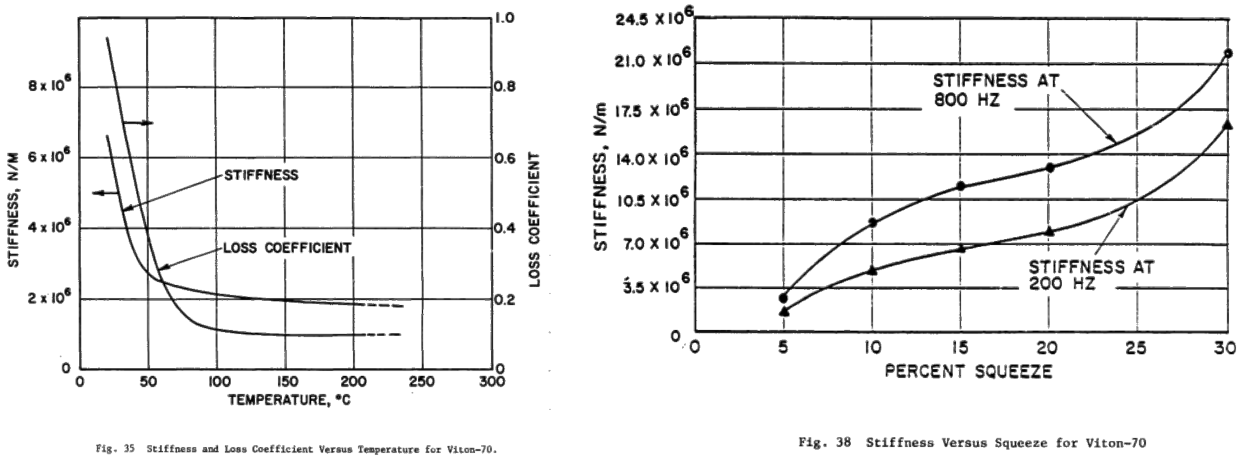

Fig. 35 Stiffness and Loss Coefficient Versus Temperature for Viton-70.

Fig. 38 Stiffness Versus Squeeze for Viton-70

Fig. 23 Sensitivity of O-ring stiffness and damping to temperature and squeeze [3]

Smalley's analysis did not incorporate scaling, as he only examined O-rings of a single outer diameter. Al-Bender et al [6] found O-ring radial stiffness and damping scaled inversely with inner diameter and cross sectional diameter. However, only two cross-sectional diameters and inner diameters were examined, and experimental measurements of stiffness and damping were found to deviate from estimates by as much as 3 times.

B. O-ring Experimental Characterization

The rotordynamic analysis presented in this chapter assumed dampers constructed from 3 Buna-N O-rings of circular cross-section, with stiffness and damping values estimated from the empirical scaling models of Al-Bender et al [6]. As these scaling models have significant error margins, an experimental characterization of the radial stiffness and damping of the O-rings to be used in the damper is necessary.

The goal of the experiment is to obtain an empirical database of O-Ring radial dynamic stiffness and damping with which the performance of a damper (consisting of up to 3 O-rings) can be predicted. This database will capture the impact of the following variables: material properties (e.g. hardness, loss coefficient), squeeze, temperature, and cross-sectional geometry. O-ring dynamic radial stiffness and damping is to be characterized up to the design operating frequency of 210 Hz. 7 dampers consisting of 7 sets of 3 identical O-rings are tested to assess the impact of each

parameter. The 7 different O-ring types are listed in Table 2. Dampers can also be constructed from a mixture of O-rings (e.g. two circular PTFE and one square Buna-N O-ring), and it is hypothesized that the performance of these 'hybrid' dampers can be modelled with all three O-rings as springs in parallel. To test this hypothesis, 3 hybrid dampers will be also similarly evaluated.

Case	Material	Hardness	Cross-section
Nominal	Buna-N	70A	Circle
Increased hardness	Buna-N	90A	Circle
Square	Buna-N	70A	Square
X-Profile	Buna-N	70A	X
Super-Resilient Viton	Viton	75A	Circle
Rigid PTFE	PTFE	55D	Circle
Soft Silicone	Silicone	50A	Circle

Table 2 Candidate O-rings for damper

Figures 24 and 25 detail the layout of the O-ring characterization experiment rig. The setup replicates the bearing housing as closely as possible, with an identical squeeze mechanism including the use of shims for control of the O-ring squeeze magnitude. The central shaft in the rig is bolted to the table, and the shakers attached to the external housing. A pair of accelerometers are epoxied to the surfaces of the housing opposite to the shakers, which measure the vibrational response. An additional pair of accelerometers are installed in the shaft (as shown in Figure 24) to check that the shaft remains rigid. 6 force sensors, 2 under each O-ring displaced 90 degrees tangentially from one another, are used to measure the radial compression forces on the O-rings (from which an equivalent squeeze value can be calculated).

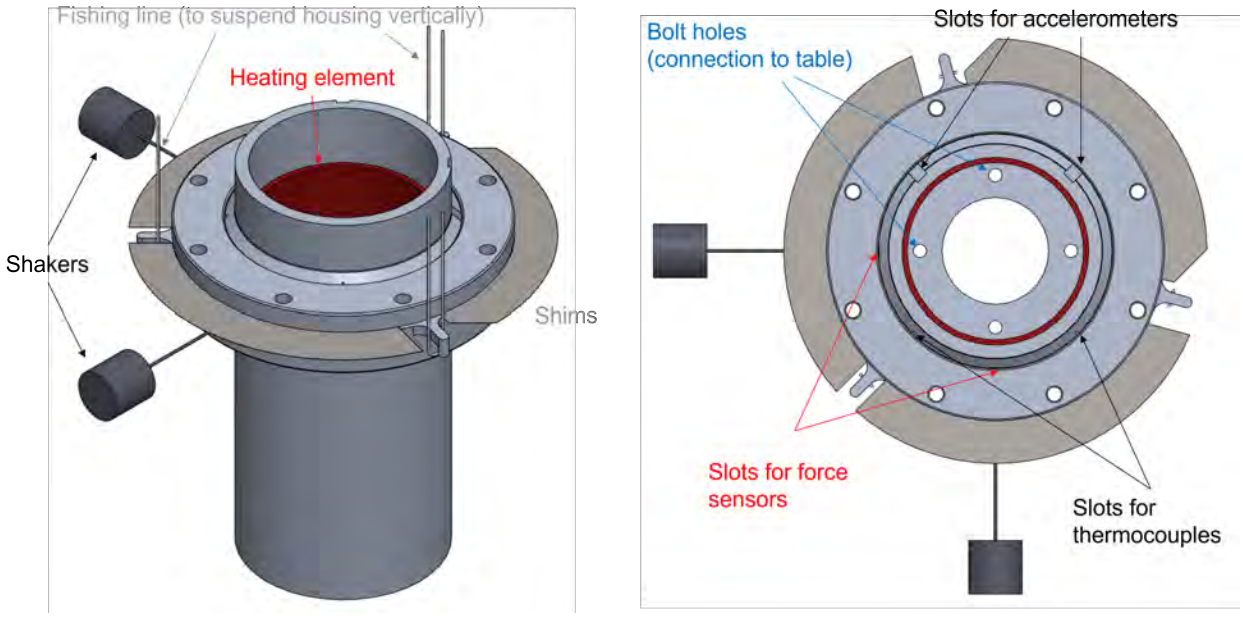

Fig. 24 Isometric view (left) and top view (right) of O-ring characterization rig

C. Full-scale Damper Tuning

The demonstrator damper system is to be experimentally tuned as a risk-mitigating step before final demonstrator assembly. One motor drive unit will be connected to an external drive, with vibrations at the bearings and change in rotor displacement measured as it is gradually brought up to design speed. If the rotordynamic performance does not meet requirements (i.e. insufficient separation margin, excessive vibrations or air gap loss), the level of damping is to

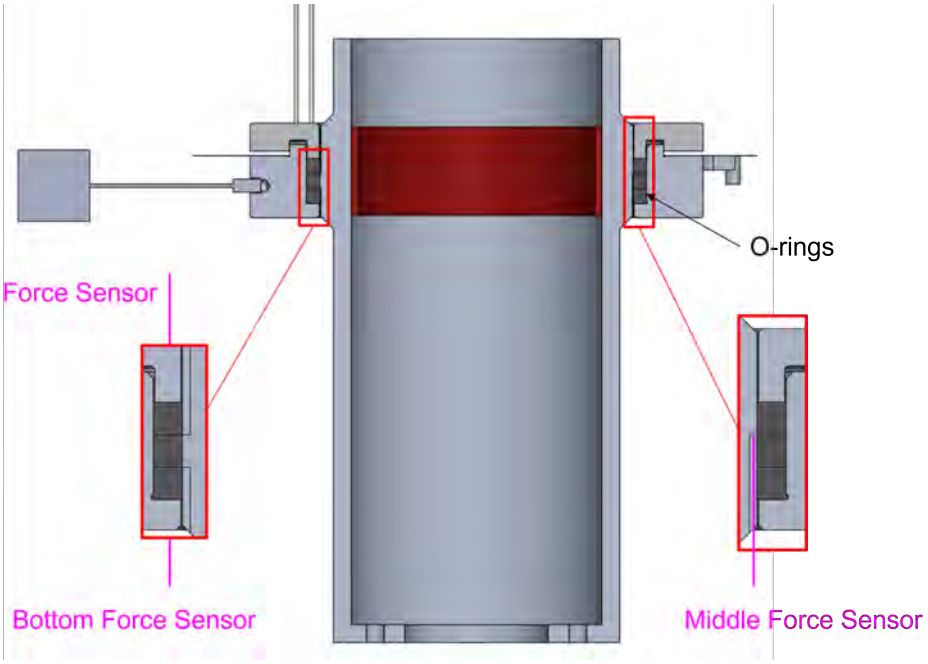

Fig. 25 Cross-sectional view of O-ring characterization rig

be modified (either through a change in squeeze setting or a replacement of O-rings) as necessary. The data obtained from the prior O-ring characterization experiments will be used to minimize the number of replacements necessary. For example, if results from the first damper tuning test suggests halving of the damper radial stiffness is required, the collected O-ring data will be referenced, and a combination of O-rings with half the radial stiffness will be used for the next test.

As O-rings have variability in thickness and size associated with manufacturing tolerances, the same squeeze settings may yield a different damper stiffness when the O-rings are replaced (as will be done when the system is disassembled and reassembled for commissioning). Therefore, to ensure the consistency of the damper performance, squeeze settings will not be relied upon during the commissioning process. Instead, the rotor frequencies are to be characterized via a ring test during the damper tuning, and during subsequent reassemblies, the rotor is to be subjected to a ring test and the damper squeeze tuned to match the previously measured frequencies.

VI. Conclusion

Electric machine scaling laws show increasing length-to-radius aspect ratio improves specific power, and one key obstacle to doing so is maintaining air-gap clearances in operation. Electric machine rotors with high flexural rigidity aid in overcoming this obstacle by minimizing the number of critical modes that must be crossed during operation. One advantage of outer-rotor machines over their inner-rotor counterparts in this respect is that for the same air gap radius, the rotor elements are at a larger radius and therefore for the same mass or thickness have significantly higher flexural rigidity (as second moment of area scales with radius to the fourth power).

Successfully managing the spindle natural frequencies in the overhung architecture is critical to system operability due to the difficulty in adding damping to these modes. While this challenge is addressed with a stiffened spindle in the demonstrator, keeping the spindle natural frequencies above design speed will be increasingly costly and difficult if rotor length-to-radius aspect ratio is further increased, and would likely mandate changing the bearing layout from an overhung rotor system to one with bearings placed both forward and aft of the electric machine. The tradeoff is the corresponding cost of increased constraints on the cooling system (including the routing of the electric machine cooling flows) and the potential impact of rotor radial growth (and correspondingly axial shrinkage) at speed on bearing preload forces.

Fluid dampers come with complexity and mass (not just of the damper itself but the associated fluid system as well), and the comparatively low damping requirements of the demonstrator present the potential to avoid these penalties with

the use of solid dampers. Successful demonstration of the tunable solid damper system, showing both predictability and in-situ control of damper parameters, would not only mitigate a key risk for the demonstrator but also present opportunities for its application to a wide range of systems where O-rings are already used for sealing purposes but additional damping is necessary, such as gas turbines.

Acknowledgments

This project is funded by Mitsubishi Heavy Industries which is gratefully acknowledged. Special thanks go to Koichiro Iida, Mikito Sasaki, and Masahiko Ezumi for their technical support and collaboration.

References

[1] Grace, K., Galioto, S., Bodla, K., and El-Refaie, A. M., "Design and Testing of a Carbon-Fiber-Wrapped Synchronous Reluctance Traction Motor," *IEEE Transactions on Industry Applications*, Vol. 54, No. 5, 2018, pp. 4207–4217. https://doi.org/10.1109/TIA.2018.2836966.

[2] Spakovszky, Z. S., Chen, Y., Greitzer, E. M., Cordero, Z. C., Lang, J. H., James L. Kirtley, J., Perreault, D. J., Andersen, H. N., Qasim, M. M., Cuadrado, D. G., Otten, D. M., and Amato, M., "A Megawatt-Class Electrical Machine Technology Demonstrator For Turbo-Electric Propulsion," AIAA/IEEE Electric Aircraft Technologies Symposium (EATS), 2023. Extended Abstract Submission.

[3] Smalley, A. J., "Stiffness and damping of elastomeric O-ring bearing mounts," NASA contract report, 1977.

[4] Spakovszky, Z. S., "Applications of axial and radial compressor dynamic system modeling," Ph.D. thesis, Massachusetts Institute of Technology, 2000.

[5] Dowdle, A., "Design of a High Specific Power Electric Machine for Turboelectric Propulsion," Ph.D. thesis, Massachussets Institute of Technology, 2022.

[6] Al-Bender, F., Colombo, F., Reynaerts, D., Villavicencio, R., and Waumans, T., "Dynamic Characterization of Rubber O-Rings: Squeeze and Size Effects," *Advances in Tribology*, Vol. 2017, 2017, pp. 1–12. https://doi.org/10.1155/2017/2509879.